ADVANCED FUNCTIONAL MATERIALS
www.afm-journal.de

Accelerated Li^+ Desolvation for Diffusion Booster Enabling Low-Temperature Sulfur Redox Kinetics via Electrocatalytic Carbon-Grazfted-CoP Porous Nanosheets

Xin Zhang, Xiangyang Li, Yongzheng Zhang, Xiang Li, Qinghua Guan, Jian Wang,* Zechao Zhuang, Quan Zhuang, Xiaomin Cheng, Haitao Liu, Jing Zhang, Chunyin Shen, Hongzhen Lin, Yanli Wang,* Liang Zhan,* and Licheng Ling*

Lithium–sulfur (Li–S) batteries are famous for their high energy density and low cost, but prevented by sluggish redox kinetics of sulfur species due to depressive Li ion diffusion kinetics, especially under low-temperature environment. Herein, a combined strategy of electrocatalysis and pore sieving effect is put forward to dissociate the Li^+ solvation structure to stimulate the free Li^+ diffusion, further improving sulfur redox reaction kinetics. As a protocol, an electrocatalytic porous diffusion-boosted nitrogen-doped carbon-grafted-CoP nanosheet is designed via forming the N–Co–P active structure to release more free Li^+ to react with sulfur species, as fully investigated by electrochemical tests, theoretical simulations and in situ/ex situ characterizations. As a result, the cells with diffusion booster achieve desirable lifespan of 800 cycles at 2 C and excellent rate capability (775 mAh g^{-1} at 3 C). Impressively, in a condition of high mass loading or low-temperature environment, the cell with 5.7 mg cm^{-2} stabilizes an areal capacity of 3.2 mAh cm^{-2} and the charming capacity of 647 mAh g^{-1} is obtained under 0 °C after 80 cycles, demonstrating a promising route of providing more free Li ions toward practical high-energy Li–S batteries.

1. Introduction

The rapid developments of various portable electronic devices and electric vehicles have put forward an urgent necessity to develop higher energy density storage systems.[1] In comparison to commercial lithium ion batteries, lithium–sulfur (Li–S) batteries output ultrahigh theoretical energy density of 2600 Wh kg^{-1}, which are considered as promising large-scale energy storage systems.[2] However, the "shuttle effect" of lithium polysulfides (LiPSs) and sluggish redox conversion kinetics of sulfur species lead to unsatisfactory interconversion rate, which results from slow Li^+ migration kinetics dissociated from large Li^+-solvation shell structure. In extreme occasion, such as low-temperature surroundings, the sever hinderance of larger Li ion solvation structure further shortens cycling life of Li–S batteries,which in turn prevents their capacities.[3]

X. Zhang, Y. Zhang, X. Li, X. Cheng, C. Shen, Y. Wang, L. Zhan, L. Ling
State Key Laboratory of Green Chemical Engineering and Industrial Catalysis
Key Laboratory of Specially Functional Polymeric Materials and Related Technology (Ministry of Education)
State Key Laboratory of Chemical Engineering
East China University of Science and Technology
Shanghai 200237, P. R. China
E-mail: zhangyongzheng@ecust.edu.cn; ylwang@ecust.edu.cn; zhanliang@ecust.edu.cn

X. Li, Q. Zhuang
Inner Mongolia Key Laboratory of Carbon Nanomaterials
Nano Innovation Institute (NII)
Inner Mongolia Minzu University
Tongliao, Inner Mongolia 028000, P. R. China

Q. Guan, J. Wang, H. Lin
i-Lab & CAS Key Laboratory of Nanophotonic Materials and Device
Suzhou Institute of Nano-Tech and Nano-Bionics, Chinese Academy of Sciences
Suzhou, Jiangsu 215123, P. R. China
E-mail: jian.wang@kit.edu

J. Wang
Helmholtz Institute Ulm (HIU)
D89081 Ulm, Germany

Z. Zhuang
Department of Chemistry
Tsinghua University
Beijing 100084, P. R. China

H. Liu
Laboratory of Computational Physics
Institute of Applied Physics and Computational Mathematics
Beijing 100088, P. R. China

J. Zhang
School of Materials Science and Engineering
Xi'an University of Technology
Xi'an, Shanxi 710048, P. R. China

The ORCID identification number(s) for the author(s) of this article can be found under https://doi.org/10.1002/adfm.202302624

DOI: 10.1002/adfm.202302624

To solve the aforementioned issues, various nanostructured materials with the functionalities of physical constraint,[4] chemical adsorption,[5] and electrocatalytic activity[6] toward LiPSs have been developed to suppress polysulfide shuttling or accelerate sulfur conversions. Although above-mentioned strategies contribute to improve the electrochemical properties, the high-rate performance and long-cycle life are still unsatisfactory and the low-temperature performance of fabricated cells is still unknown. Considering the complexity of sulfur redox conversions,[7] the sulfur utilization is closely related with the insertion/extraction amount of free Li ions and most strategies have ignored the desolvation processes of solvated Li^+ at the electrode/electrolyte interface, which inevitably lowers the migration of Li^+ and thus reduces the conversion kinetics of sulfur species.[8] In typical ether electrolytes, Li^+ is generally associated with solvents, such as dimethyl ether, forming the solvation sheath with large size.[9] To a certain extent, such a solvation structure would bring about the occurrence of co-insertion into cathode, deteriorating the stability of cathode structure.[10] More efforts have also been devoted to ameliorating the electrolyte to modulate outer anion-involved solvation sheath. For example, the application of high concentration electrolyte (>3 M) could significantly improve the ratio of anions to solvents in the electrolyte and realize the entry of anions into the solvation sheath.[11] On the other hand, the constructions of porous morphology with sieving effect, i.e., metal–organic frameworks (MOFs), and covalent organic frameworks (COFs), have been demonstrated effectively for fast desolvation.[12] However, the heavy utilization of electrolyte salt burdens the cost and the electrochemical instability of MOFs and COFs would make poor desolvation capability in the later cycles.

Beyond conditioning the engineering of electrolyte or poor morphology, recently, the emerging electrocatalysis is proposed to facilitate the dissociation of Li^+-solvents to release more free Li ions. For example, our group indicated that a MOF-Carbon bridged catalytic network is beneficial for promoting the formation of anion-involved Li^+ solvation structure, catalyzing the Li^+-solvents dissociation kinetics and providing a fast channel for Li^+ transport.[13] As pointed above, owing to the instability of MOFs and the lack of active sites, the strategy might fail in the low-temperature environments, limiting the dissociation of solvent molecules from the solvation sheath of cations, which is detrimental to the catalytic efficiency of obtaining free Li ion to propel polysulfide conversions. Therefore, designing a stable yet highly catalytic layer to accelerate the dissociation of Li^+-solvents in low-temperature environment is of great significance to generate more free Li ions to facilitate sulfur redox reaction kinetics.

Herein, a combined functionality of electrocatalysis and pore sieving effect originated from electrochemical porous nanosheets is proposed to accelerate the dissociation of Li^+-solvent molecules, driving to release large numbers of free Li^+ to promote the redox kinetics of sulfur species and to further improve the utilization. Concretely, taking advantages of nitrogen-doped carbon grafted porous CoP with electrocatalytic effect, a Li^+ diffusion booster (EPDB-CgCP) is programmed to catalyze Li^+ desolvation or sieve large size solvent molecules. As revealed by in situ/ex situ characterizations, theoretical simulations and electrochemical detections, the EPDB-CgCP facilitates the desolvation effect with higher Li ion conductivity and Li^+ transference number. Encouraged by these merits, the Li–S cells with EPDB-CgCP ion diffusion booster provide an excellent rate capability (775 mAh g^{-1} at 3 C) and a promising life expectancy with a low specific capacity decay of 0.048% per cycle after 800 cycles at 2 C. Especially under a severe condition of high mass-loading or low-temperature environment, the cell with EPDB-CgCP maintains a respectable areal capacity of 3.2 mAh cm^{-2} at an ultrahigh sulfur addition of 5.7 mg cm^{-2} and a fascinating capacity of 647 mAh g^{-1} under the low temperature of 0 °C after 80 cycles, paving the way for the practical use of high-efficiency Li–S batteries.

2. Results and Discussion

The synthesis procedure of the electrocatalytic porous nitrogen-doped carbon-grafted-CoP nanosheets diffusion booster (EPDB-CgCP) is illustrated in **Figure 1**A. In detail, with the aid of 2-Methylimidazole (2-MIM) ligand, the Co-based precursors transform to form hexagonal nanosheets under a mediating effect of the cetyltrimethylammonium bromide (CTAB) surfactant via a self-assembly method. Subsequently, after a solid/gas-phase phosphorization reaction in Ar atmosphere under high temperature, the porous nitrogen-doped carbon-grafted-CoP nanosheets diffusion booster is obtained with the formation of N–Co–P active structure. The scanning electron microscopy (SEM) images in Figure S1 (Supporting Information) show that the as-prepared precursor exhibits a highly uniform smooth hexagonal structure. After different annealing conditions, both the EPDB-CgCP (Figure 1B) and the controlled carbon-grafted CoO (CgCO) (Figure S2, Supporting Information) retain the regular hexagonal morphology with different pore sizes in the range of 50–100 nm. In the transmission electron microscopy (TEM) images (Figure 1C), the pore on the nanosheet is obvious and a lattice fringe of 0.282 nm is observed, which is consistent with the (011) crystal plane of CoP.[14] Furthermore, distinct interfaces between CoP and nitrogen-doped carbon coating are identified in Figure S3 (Supporting Information). The energy-dispersive spectroscopy (EDS) mapping results present homogeneous elemental distributions of Co, P, and N in the as-fabricated EPDB-CgCP (Figure 1D). The X-ray powder diffraction (XRD) patterns in Figure 1E clearly demonstrate the successful transformation to EPDB-CgCP and CgCO with/without phosphorization, respectively. The N_2 adsorption–desorption isotherms of EPDB-CgCP and CgCO were characterized. In comparison with the CgCO, the EPDB-CgCP displays a decreased specific surface area, which might be ascribed to the heavier weight of CoP at equal mole amount than that of CoO in CgCO (Figure S4A, Supporting Information). In contrast to the larger pore sizes in CgCO, mesopores and micropores dominate after phosphorization (Figure S4B, Supporting Information), which facilitates the sieving effect on solvated lithium ions at the sub-nanometer level (from 0.2 to ≈1 nm).[12,15] To ascertain the bonding chemical surroundings, X-ray photoelectron spectroscopy (XPS) was conducted (Figure S5A, Supporting Information). In the high-resolution Co 2*p* spectrum of EPDB-CgCP (Figure 1F), the peaks located at 778.7 and 793.7 eV can be attributed to Co–P bonds in EPDB-CgCP,[16] which corresponds well to the peaks at 130.0 (P 2*p*1/2) and 129.2 eV (2*p*3/2) in the P 2*p* deconvoluted sub-spectra (Figure 1G).[17] Notably, a pair of peaks come out at 783.2 and 799.3 eV, which are ascribed to the formation of Co–N bonds

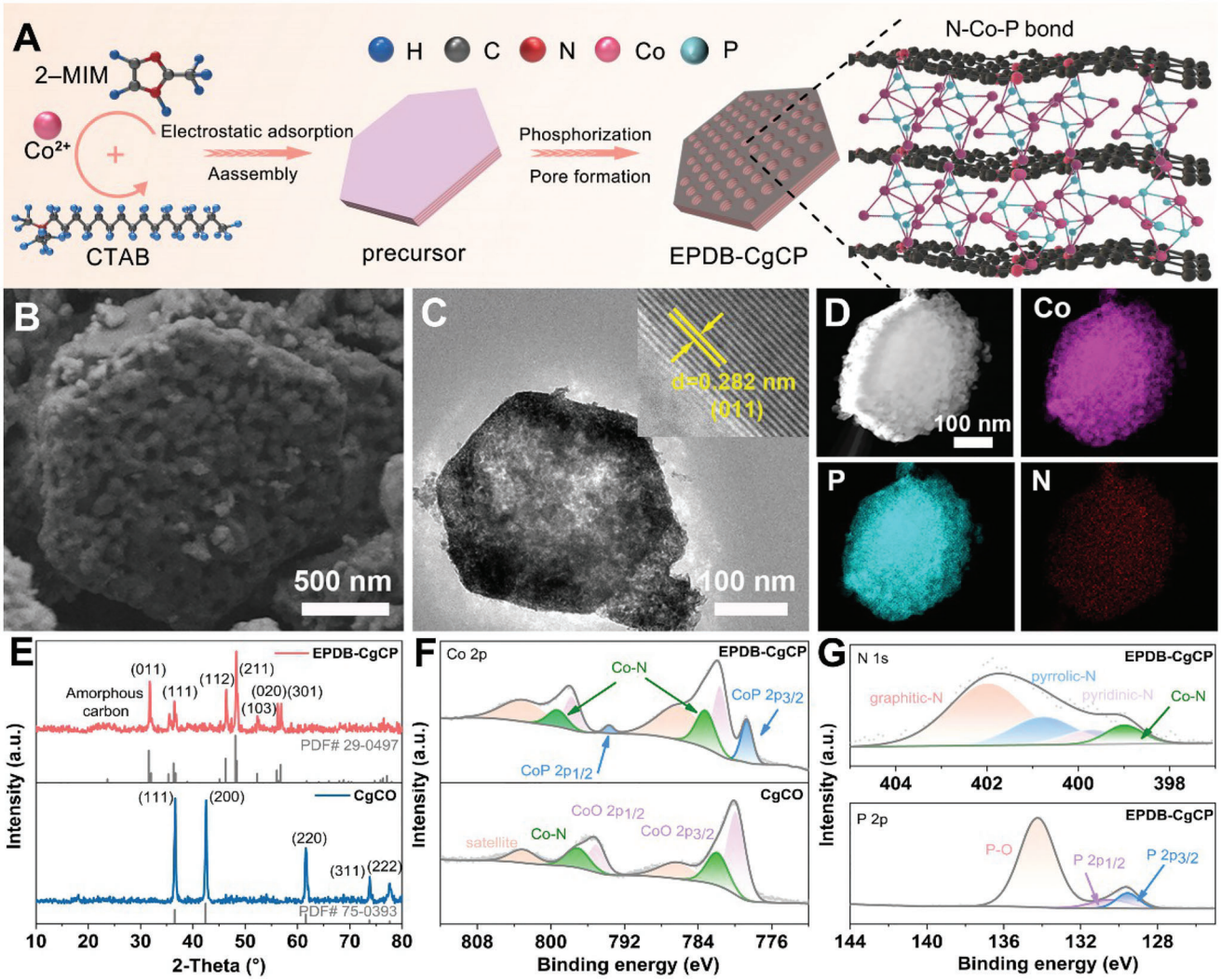

Figure 1. A) Schematic illustration for the preparation of EPDB-CgCP. B) SEM and C) TEM and lattice images of EPDB-CgCP. D) The elemental mapping images of EPDB-CgCP. E) XRD patterns of EPDB-CgCP and CgCO. F) Comparison of high–resolution Co 2*p* spectra in the EPDB-CgCP and CgCO. G) High–resolution spectra of N 1*s* and P 2*p* in the EPDB-CgCP.

during pyrolysis.[18] The Co–N bonds shift toward the direction of high binding energy compared to the Co–O bonds, which might be ascribed to the generation of a high catalytic active site for Co–N_x species.[19] Meanwhile, the peak at 399.0 eV in the high-resolution XPS spectra for N 1*s* (Figure 1G; Figure S5B, Supporting Information) is also assigned to Co–N bond. Figure S5C (Supporting Information) displays the fitting peak centered at 286.6 eV is assigned to C–N bond, illustrating the forming of N-doped carbon nanosheets.[20] These results comprehensively demonstrate a chemical interaction between CoP and the N-doped carbon nanosheets with the network formation of P–Co–N–C active structure.

In typical ether-based electrolyte, additional energy is required to remove the solvent sheath and generate free Li^+ at the electrode/electrolyte interface. Briefly, as illustrated in **Figure 2**A, the desolvation behaviors can be interpreted into two aspects. On the one hand, the larger cluster of Li^+-solvents are decomposed directly by the electrocatalytic effect of bridged N–Co–P bonds on the surface, allowing the released bare Li^+ to cross the pores with a faster diffusion kinetics to participate in the catalytic conversion reaction of LiPSs. On the other hand, the outer solvation sheath layer can be sieved when these large-sized solvated Li^+ complexes pass through the penetrating pores of EPDB-CgCP. Consequently, the bare free Li ions participate and accelerate the sulfur redox kinetics with lower barriers. To confirm this, Raman investigation and a series of kinetic experiments were performed. As well known, the conventional electrolyte usually exhibits three kinds of ion structures, i.e., solvent separated ion pair (SSIP), contact ion pair (CIP), and aggregate (AGG).[21] As shown in Figure 2B, commercial liquid electrolyte (LE) in the systems with pure PP, CgCO, and EPDB-CgCP were carried out by Raman, respectively. In commercial electrolyte system with PP, the main peak is located at 741 cm^{-1} (free $TFSI^-$, one anion pairs with zero Li^+), while this peak moves toward the CIP (one anion pairs with one Li^+) at 744 cm^{-1} and AGG (one anion pairs with two or more Li^+) at 749 cm^{-1} with the introduction of EPDB-CgCP,

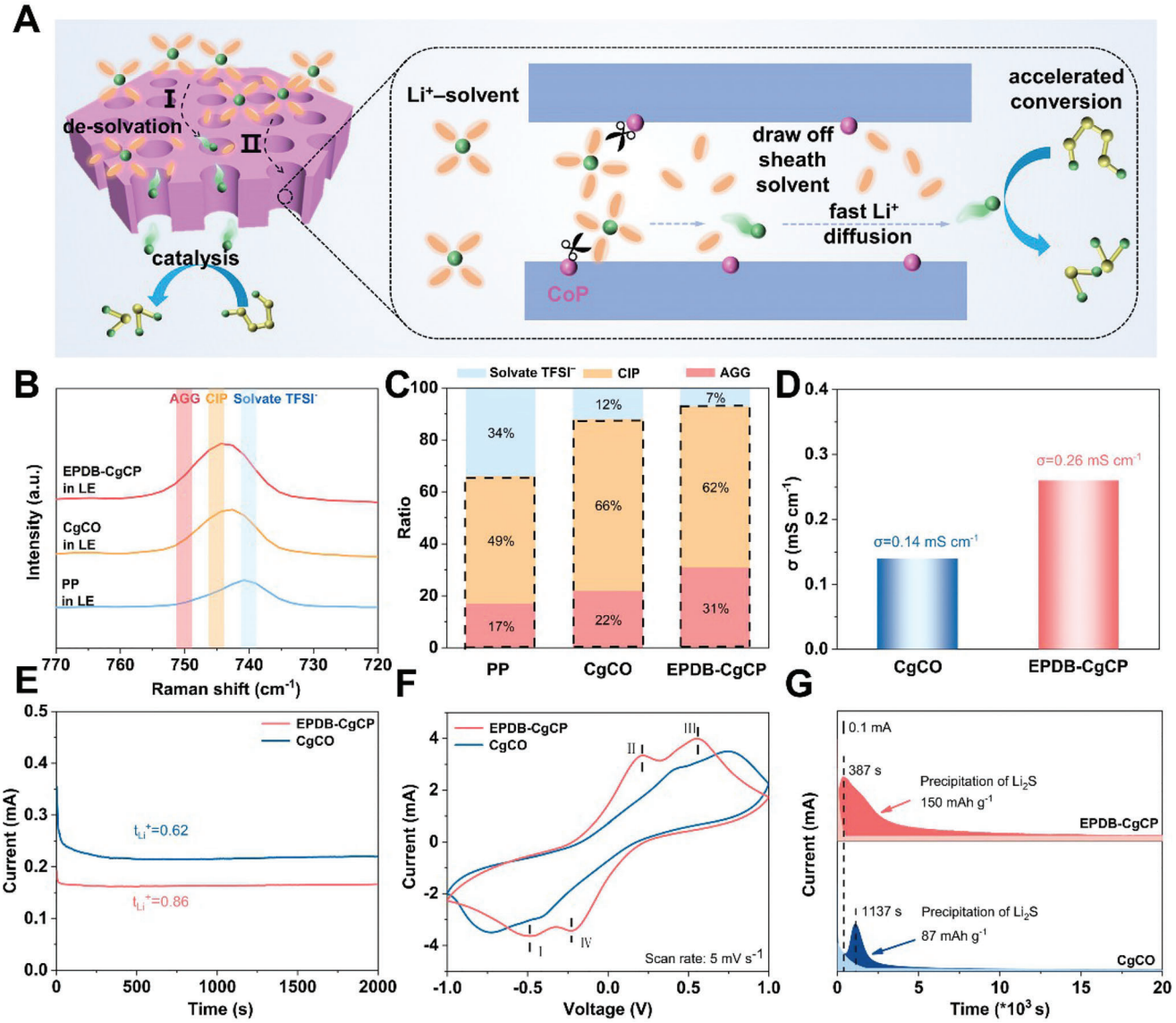

Figure 2. A) Schematic illustration of desolvation behaviors catalyzed or sieved by EPDB-CgCP. B) Comparisons of Raman spectra of the ether electrolyte with/without EPDB-CgCP. C) The ratio summary of Solvate TFSI$^-$, CIP, and AGG in different systems. Comparisons of D) ionic conductivity and E) Li^+ transference number under the two systems. F) CV curves of Li_2S_6 symmetric cells based on EPDB-CgCP and CgCO electrodes at 5 mV s^{-1}, respectively. G) Potentiostatic discharge profiles at 2.05 V on the two modified electrodes with Li_2S_8 catholyte.

implying the variation of solvation structure of the Li^+.[22] As summarized in Figure 2C, EPDB-CgCP system displays the highest overall ratios of AGGs+CIPs (93%), much higher than CgCO system (88%), and pure PP system (66%), suggesting the rapid desolvation behaviors propelled by EPDB-CgCP. Later, the effect of EPDB-CgCP on Li^+ diffusion kinetics through sieving and tailoring of solvent molecules is also evaluated by ionic conductivity (σ) (Equation S1, Supporting Information) and Li^+ transference number (t_{Li^+}) (Equation S2, Supporting Information).[23] As exhibited in Figure 2D, the ionic conductivity in the EPDB-CgCP system is determined to be 0.26 mS cm^{-1}, which is about two times higher than that in CgCO system (0.14 mS cm^{-1}). Meanwhile, the Li^+ transference number is greatly enhanced from 0.62 of CgCO to 0.86 of EPDB-CgCP (Figure 2E).[24] The apparent ion diffusion kinetic improvements are undoubtfully attributed to simultaneously electrocatalytic and sieving effects of EPDB-CgCP.[25] Subsequently, to give insights into the effect of formed free Li^+ on sulfur redox reactions, polysulfide conversion and Li_2S precipitation experiments were performed. As demonstrated in electrochemical impedance spectroscopy (EIS) measurements (Figure S6A, Supporting Information), the charge transfer resistance for EPDB-CgCP is much smaller than that of CgCO (59 vs 101Ohm), indicating the charge transfer is substantially faster with the bridged EPDB-CgCP network.[26] Meanwhile, the symmetric cell based on pristine EPDB-CgCP electrode demonstrates higher peak currents with lower polarization than that cell with CgCO electrode in the cyclic voltammetry (CV) curves (Figure 2F), confirming the facilitation of Li^+ migration ki-

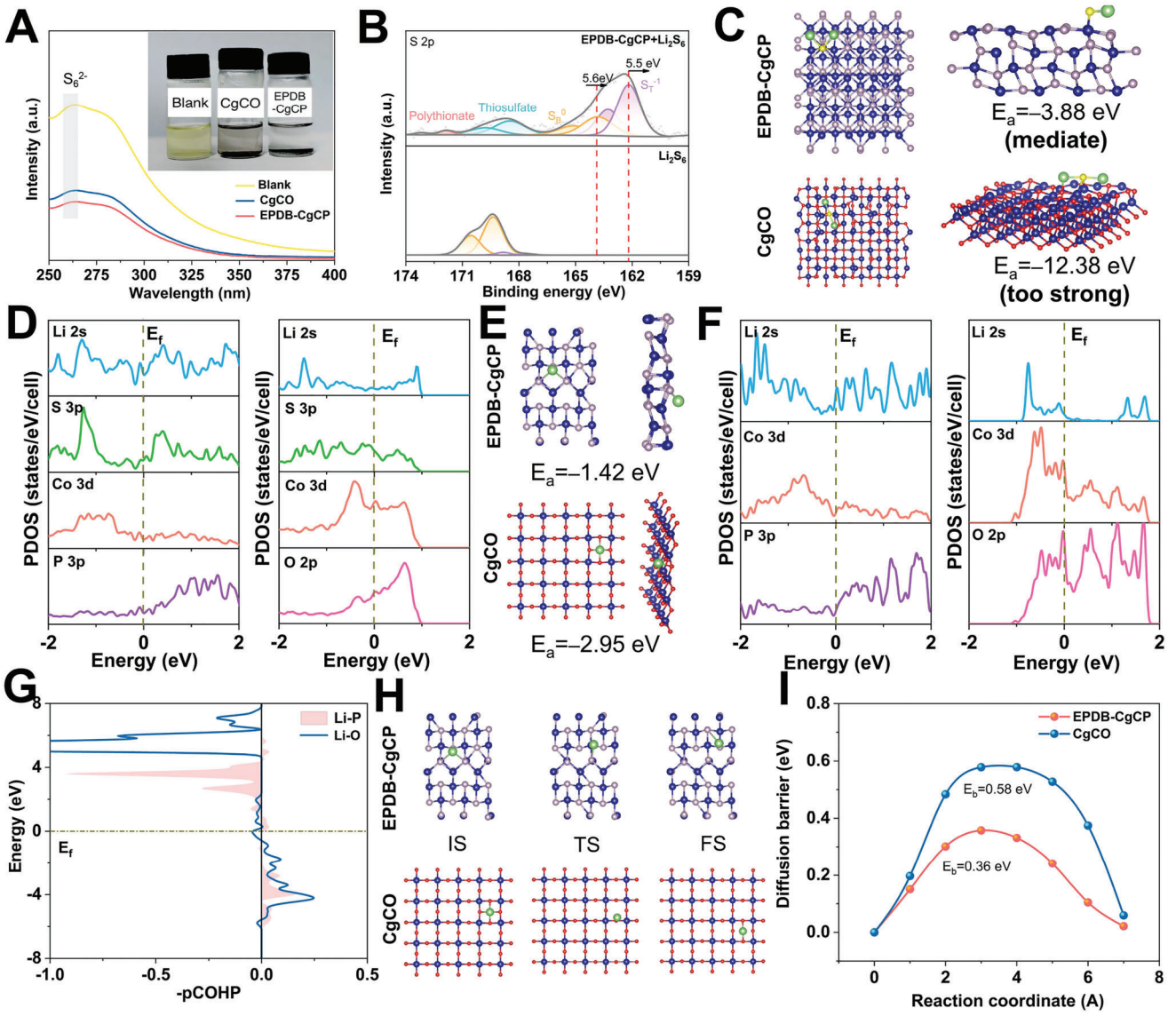

Figure 3. A) Comparison of UV–vis spectra of Li_2S_6 solution adsorbed by EPDB-CgCP and CgCO (inset figure: optical image of Li_2S_6 adsorption test). B) High resolution XPS spectra of S 2*p* for EPDB–CgCP after and before Li_2S_6 adsorption. C) Schematic diagrams of the atomic structures of EPDB-CgCP and CgCO from different views after Li_2S adsorption. D) Comparison of PDOS between EPDB-CgCP and CgCO adsorbed by Li_2S. E) Schematic diagrams of the atomic structures of EPDB-CgCP and CgCO from different views after Li^+ adsorption. F) Comparison of PDOS between EPDB-CgCP and CgCO adsorbed by Li^+. G) Comparison of COHP calculation results for EPDB-CgCP and CgCO. H) Schematic diagrams of the atomic structures of EPDB-CgCP and CgCO in different states. I) Comparison of the migration potential energy of Li^+ on EPDB-CgCP or CgCO surface.

netics owing to the numerous free Li^+ from the solvation structure catalyzed by EPDB-CgCP.[27] Figure 2G reveals that the cell with EPDB-CgCP electrode and Li_2S_8 catholyte presents not only a shorter time to reach the peak current (387 s), but also a higher capacity of Li_2S precipitation (150 mAh g^{-1}) compared to the cell with CgCO electrode (1137 s, 87 mAh g^{-1}), indicating the fast formation of Li_2S on the EPDB-CgCP by the aid of free Li^+.[28] In the dissolution process (Figure S6B, Supporting Information), the peak of the cell with EPDB-CgCP electrode appears much earlier (844 s) than that of CgCO (1731 s) with higher current intensity as well, reaffirming superior reversible performance due to fast Li^+ kinetics. In the cycled electrode, it is obvious that the large amount of Li_2S is uniformly deposited on the surface of EPDB-CgCP electrode (Figure S6C, Supporting Information) while it is random on CgCO electrode (Figure S6D, Supporting Information), indicating the enhanced utilization of sulfur by EPDB-CgCP.[29]

To explore the function of EPDB-CgCP on polysulfides, a static adsorption experiment of Li_2S_6 solution (0.2M) was conducted. As can be seen from the inset of **Figure 3**A, after sufficient interaction for 6 h, the Li_2S_6 solution with EPDB-CgCP becomes clearer and even transparent compared to the initial solution. Successively, the UV–vis spectra display that the absorption peaks of S_6^{2-} species at ≈264 nm are the weakest one (Figure 3A),

suggesting the majority of polysulfides have been conversed by EPDB-CgCP.[6a] Subsequently, the special chemical interactions between EPDB-CgCP and LiPSs were studied by XPS analysis. As indicated in Figure S7A (Supporting Information), a new peak attributed to Li–P bond appears at 55.7 eV, demonstrating the binding ability of EPDB-CgCP with Li_2S_6.[30] In the S 2*p* spectra (Figure 3B), a more pronounced shift of the absorption peak toward the lower binding energy appears and a significant bond of Co–S forms, indicating a relatively strong interaction between EPDB-CgCP and Li_2S_6.[31] In addition to a negative shift of ≈0.6 eV observed in the Co 2*p* spectra (Figure S7B, Supporting Information), more remarkably, a new peak at 777.3 eV attributed to a chemical bond-like Co–S bond can greatly demonstrate the chemical interaction capability and further suppress the shuttle effect.[17,32] The same negative shift in binding energy can also be evidently observed in the P 2*p* spectra (Figure S7C, Supporting Information).

To theoretically verify robust chemical interactions, the relationships between polysulfide or Li ion and EPDB-CgCP or CgCO were calculated, respectively. The adsorption structures of Li_2S on EPDB-CgCP and CgCO are exhibited in Figure 3C. As far as we know, the too strong adsorption would tend to catch the active materials tightly, which is inferior to the further chemical transformation. The enormous binding energy of −12.38 eV (Equation S3, Supporting Information) for CgCO case indicates the poisoning of Li_2S on CgCO surface, while EPDB-CgCP possesses the mediate adsorption energy (−3.88 eV),[33] which enables EPDB-CgCP to participate in and refresh further catalytic conversion of Li_2S_6 in the adsorption test of polysulfide, resulting in lower concentrations of Li_2S_6 in the solution. As elucidated in the projected density of states (PDOS) images (Figure 3D), hybridization between Co_3*d* and S_3*p* orbitals after adsorbing Li_2S is obvious. However, for the CgCO case, the newly hybridization of O_2*p* and Li_2*s* dominates the interactions between CgCO and Li_2S, proving that the interactions of EPDB-CgCP and Li_2S to form the Co–S bond. To verify the mobility of Li^+, the electronic properties and Li^+ diffusion across the EPDB-CgCP and CgCO were analyzed. The optimized structures display that the Li^+ is located above the surface of EPDB-CgCP, while Li^+ is strongly adsorbed into the surface by oxygen atoms for CgCO (Figure 3E), forming different binding modes. Similarly, PDOS images illustrate that the *s* orbitals of Li and the *p* orbitals of P below the Fermi energy level are crosslinked to a weaker extent and weakly hybridized, which can implement the Li desorption more effectively (Figure 3F). To further determine the strength of chemical bonds and to quantify the bonding strength, crystal orbital Hamilton population (COHP) analyses are disclosed (Figure 3G). Obtained from the comparison of the curves in the occupied bound states (–COHP>0), Li–O possesses an enhanced bonding ability compared to Li–P, demonstrating a stronger Li–O bond formation and inhibiting the possible Li ion diffusion. In this way, the diffusion barrier of Li^+ on the surface of EPDB-CgCP and CgCO were compared and shown in Figure 3H,I. The dramatic reduction of the energy barrier displays that EPDB-CgCP provides more exceptional electrochemical properties and more encouraging Li^+ migration kinetics (0.36 vs. 0.58 eV), significantly demonstrating the capability of EPDB-CgCP in boosting ion diffusion for high-efficient sulfur redox kinetics.[34]

To evaluate the electrochemical performances in sulfur cathode, 2025-type coin cells with EPDB-CgCP and CgCO modified separators (noted as EPDB-CgCP@PP and CgCO@PP, respectively) were assembled, respectively. As depicted in the CV profiles (Figure S8A, Supporting Information), the cell with EPDB-CgCP ion diffusion booster delivers higher reduction potentials with the smaller potential hysteresis than that of CgCO@PP, indicating the driving effect of EPDB-CgCP on the conversion kinetics of sulfur redox due to the promising Li^+ diffusion.[35] To better visualize the catalytic effect of the EPDB-CgCP accelerator, the differences in Tafel slopes (**Figure 4**A; Figure S8B, Supporting Information) were analyzed according to the two reduction peaks (I and II).[36] During the sulfur reduction reactions, the cell with EPDB-CgCP exhibits smaller Tafel slopes (90 and 89 mV dec^{-1}) than that with CgCO (118 and 128 mV dec^{-1}) thanks to its accelerated Li^+ dissociation ability.[37] Similarly, the enhanced migration of Li^+ can be investigated from the corresponding diffusion coefficient of Li^+ (Equation S4, Supporting Information) through galvanostatic intermittent titration technique (GITT). As shown in Figure 4B and Figure S9 (Supporting Information), the migration rate of Li^+ is accelerated with the electrocatalytic action of EPDB-CgCP during charge and discharge processes.[38] Thanks to the accelerated Li^+ desolvation of the diffusion booster, the cell with EPDB-CgCP@PP unsurprisingly delivers a higher initial discharge capacity of 1169 mAh g^{-1} at 0.2 C than the cell with CgCO@PP (967 mAh g^{-1}) and a smaller polarization potential ($\Delta V = 181$ mV) (Figure 4C). With a detail analysis, the cell with EPDB-CgCP@PP displays a higher Q_L/Q_H ratio (2.5 vs. 2.0), indicating a progressive sulfur utilization.[39] After 100 cycles, the cell with EPDB-CgCP@PP displays a capacity of 899 mAh g^{-1}, higher than that of 731 mAh g^{-1} in the CgCO@PP system (Figure 4D). It is worth noting that the EPDB-CgCP composite shows negligible Li ion storage ability (Figure S10, Supporting Information). Figure 4E displays the Li–S cell with EPDB-CgCP@PP delivers discharge capacities of 1159, 1022, 922, 826, and 775 mAh g^{-1} at 0.2, 0.5, 1, 2, and 3 C, respectively, while the cell with CgCO@PP only exhibits 244 mAh g^{-1} at a higher current rate of 3 C, much lower than that with EPDB-CgCP@PP, implying the outstanding contribution of EPDB-CgCP electrocatalyst for forming rapid ion diffusion to the enhanced performance.[40] In addition, the overpotential gaps at different rates were also summarized for comparison. As displayed in Figure 4F and Figure S11 (Supporting Information), the overpotential gaps increase slowly with the ion diffusion booster propelled by EPDB-CgCP. However, for the CgCO one, the discharge plateau of the cell seems lost and the overpotential gap is enlarged as higher as 811 mV at 3 C. In the long-term cycles at 2 C, the fast generation and movement of Li^+ boost the cell with EPDB-CgCP@PP to deliver an initial capacity of 833 mAh g^{-1} and a desirable lifespan of 800 cycles at 2 C with a low fading rate of 0.048% per cycle (Figure S12, Supporting Information).

High mass-loading and low temperature tolerance are the two main obstacles to realize the commercial potential of Li–S batteries. To reveal the superiority of the EPDB-CgCP electrocatalyst for the high sulfur loading cell, favorable capacities of 990, 850, 634, and 517 mAh g^{-1} are preserved under a sulfur loading of 3.0 mg cm^{-2} from 0.1 to 1 C (Figure 4G). Evaluating the sulfur loading up to 5.7 mg cm^{-2} (Figure 4H; Figure S13, Sup-

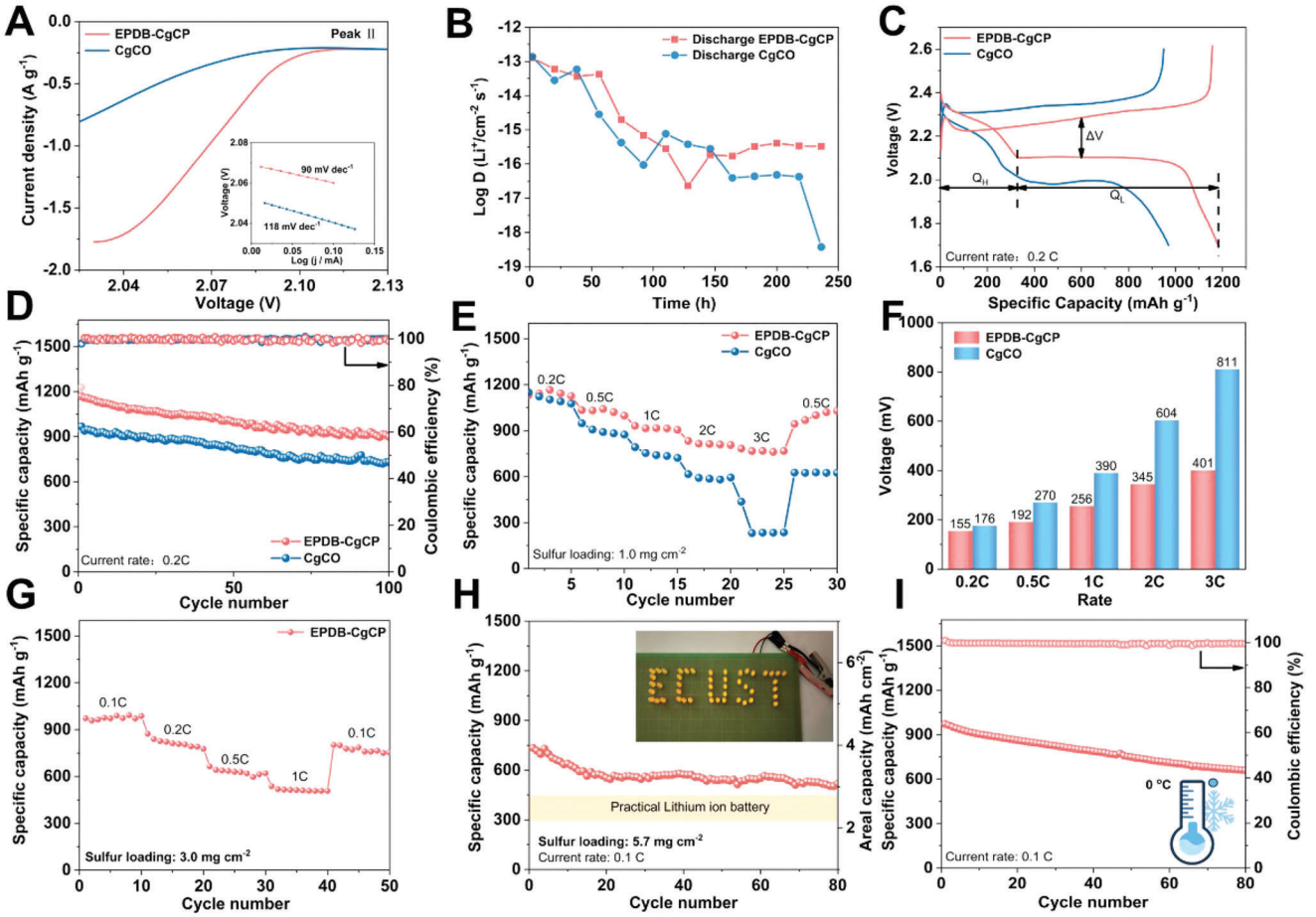

Figure 4. A) The corresponding Tafel plots derived from CV curves. B) Diffusion coefficients of Li^+ in the discharge process. C) Voltage curves and D) cycling performance of the two cells with EPDB-CgCP or CgCO at 0.2 C. E) Rate performance of EPDB-CgCP and CgCO modified cells. F) Comparison of overpotential gaps at different rates. G) Rate performance of high−mass−loading cell (3.0 mg cm^{-2}) with EPDB-CgCP. H) Cyclic performance of the cell employed with a high sulfur loading up to 5.7 mg cm^{-2} with EPDB-CgCP at 0.1 C. I) Cyclic performance of EPDB-CgCP modified cell at 0.1 C under a low−temperature environment of 0 °C.

porting Information), the fabricated cell exhibits an initial capacity of 4.0 mAh cm^{-2} (734 mAh g^{-1}) at 0.1 C and stabilizes a capacity of 3.2 mAh cm^{-2} (522 mAh g^{-1}) for 80 cycles. Meanwhile, the high-capacity cell is capable to provide a stable power supply for an electric LED lamped with "ECUST" (Figure 4H inset), demonstrating a considerable energy storage ability. Subsequently, the separators for the cell with high sulfur loading up to 5.7 mg cm^{-2} before and after cycling were subjected to SEM analyses. Compared to the original separator (Figure S14A, Supporting Information), the cycled EPDB-CgCP@PP is morphologically unchanged and EPDB-CgCP material still fits tightly to PP without any collapse (Figure S14B, Supporting Information). Meanwhile, the CV profiles were similarly applied to demonstrate the improved sulfur redox kinetics under a high sulfur loading (Figure S15, Supporting Information). Considering the low-temperature Li–S batteries are closely affected by the hinderance effect of large solvated Li ions and also restricted by the ion diffusion kinetics in harsh environment, the cell with EPDB-CgCP diffusion booster was tested at a temperature as low as 0 °C (Figure 4I; Figure S16, Supporting Information). The fabricated cell initially exhibits a charming specific capacity of 972 mAh g^{-1} at 0.1 C and stabilizes an exceptional specific capacity of 647 mAh g^{-1} for 80 cycles. Alternatively, the CV test was designed to specify the elevated redox kinetics of sulfur species due to facilitated Li^+ diffusion kinetics by EPDB-CgCP diffusion booster at low temperature down to 0 °C (Figure S17, Supporting Information). These results strongly reveal that the EPDB-CgCP is well able to promote the formation and migration of free Li^+ at both room temperature and low temperature, thus inhibiting the shuttle effect and propelling the redox conversion reactions.

In order to further probe the catalytic mechanism, in situ Raman spectroscopy tests were implemented. The structure configuration of the Li–S cell is exhibited in **Figure 5**A. The time-resolved Raman spectra of Li–S battery based on PP separator (Figure 5B,C) during discharge process at 0.2 C reveal that three Raman characteristic peaks attributed to Li_2S_8 are identified at 150, 216, and 482 cm^{-1} at the beginning of the discharge process (at ≈2.3 V).[41] Further discharged to 2.18 V, the Raman peaks of Li_2S_8 located at 150 and 216 cm^{-1} progressively disappear, while other two strong Raman peaks (at 401 and 452 cm^{-1}) corresponding to Li_2S_6 and Li_2S_4 + Li_2S_5 start to emerge, respectively. Under a fully discharged state, the intensities of some characteristic

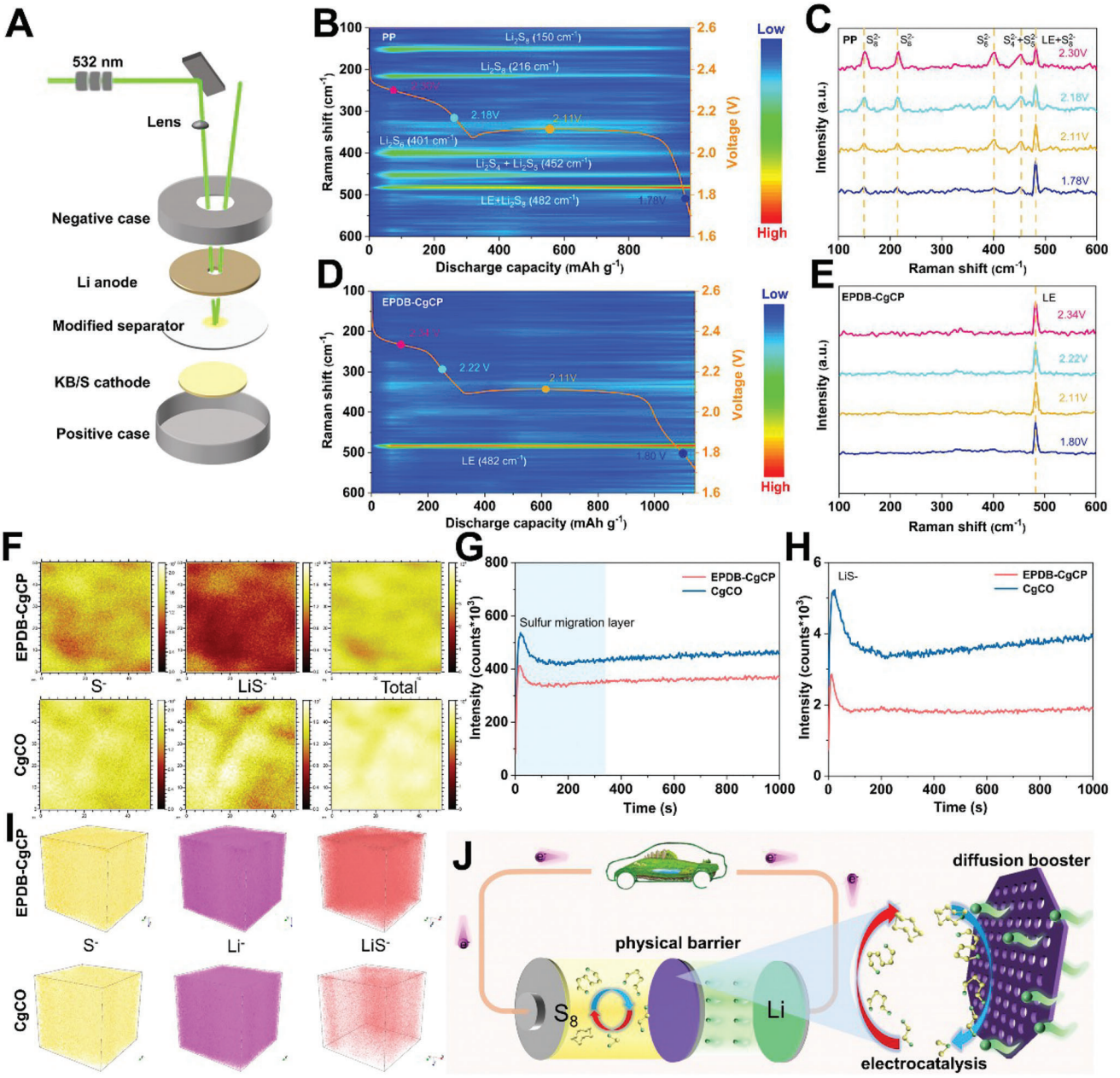

Figure 5. A) Schematic illustration of in situ Raman for Li–S battery. In situ time–resolved Raman spectra obtained during the discharge process with B) PP and D) EPDB-CgCP modified separators. The orange curves represent the discharge process. Selected Raman spectroscopy of Li–S cells based on C) PP and E) EPDB-CgCP modified separators. F) ToF–SIMS S^-, LiS^-, and total mappings on the top surfaces of the cells with EPDB-CgCP and CgCO. ToF–SIMS G) S^- and H) LiS^- depth profiles after 10 cycles at 0.2 C. I) 3D rendering secondary ions depth profile images of the cycled cells with EPDB-CgCP and CgCO. J) Illustrated mechanism of the EPDB-CgCP to accelerate sulfur redox kinetics.

peaks diminish quickly except for the peak at 482 cm^{-1}, which should be ascribed to the ingredients in liquid electrolyte (LE) (Figure S18, Supporting Information). In contrast, with EPDB-CgCP ion diffusion booster, weak Raman signals of Li_2S_8, Li_2S_6 and Li_2S_4 + Li_2S_5 are detected throughout the discharge process except for the peak at 482 cm^{-1} induced by the electrolyte (Figure 5D,E), indicating relatively fast interactions and conversions between EPDB-CgCP and LiPSs.

To trace the evolution and distribution of polysulfides, the cells with EPDB-CgCP was executed after being fully discharged by the measurement of time-of-flight secondary-ion mass spectroscopy (ToF-SIMS; Figure 5F–I). As displayed in Figure 5G,H, in comparison with the intensities of S^- and LiS^- secondary ions in the EPDB-CgCP-based cell cathode, the cell cathode with CgCO@PP presents higher intensities of the S^- and LiS^- species either at the beginning or in the later. Meanwhile, as depicted

in 2D specie distribution images, the cell with CgCO@PP exhibits bright and higher intensity in the selected area. Therefore, the total ions on the surface of the cathode with CgCO@PP present a higher polysulfide concentration aggregation on the surface, indicating that polysulfide shuttle is significantly inhibited by EPDB-CgCP with the ability of fast ion diffusion booster to rapidly converse polysulfides.[42] Subsequently, the depth analyses and 3D distribution of the S^- and LiS^- species were further analyzed (Figure 5I). Apparently, more S^-, Li^+, and LiS^- secondary ion species are restricted in the cathode interior with uniform distribution in the EPDB-CgCP system. In sharp contrast, the LiS^- species in the CgCO system display a random distribution, demonstrating that the cathode using EPDB-CgCP booster could also uniformize the Li_2S evenly.[43] These results strongly confirm the EPDB-CgCP electrocatalysis improves the desolvation kinetics for fast conversions of sulfur species. Subsequently, the catalytic and pore sieving functions of EPDB-CgCP on sulfur species by rapid desolvation to generate Li^+ are visually illustrated by a schematic diagram (Figure 5J). First, EPDB-CgCP acts as a physical barrier to LiPSs, which suppresses the shuttle effect to a certain extent. Second, the EPDB-CgCP provides electrocatalytic and sieving functions for dissociating Li^+-solvents and releasing free Li^+. Finally, the abundant reactive sites tailor the large-sized solvent molecules and accelerate the diffusion of bare Li^+ to the sulfur cathode, allowing more Li^+ to participate in the conversion processes of LiPSs, thus ultimately catalyzing the conversion of sulfur species in Li–S chemistry.

3. Conclusion

In summary, the electrocatalytic porous N-doped carbon grafted CoP nanosheets are synthesized to facilitate the dissociation of Li^+-solvents for releasing free Li^+ to propel sulfur redox conversion kinetics, especially in low-temperature environment. The structure with penetrating pores has a physical screening effect on sieving the solvent molecules while CoP provides chemical electrocatalytic sites in tailoring and dissociating the solvation sheath to promote rapid Li^+ transport, as comprehensively investigated by spectroscopical and electrochemical tests, and theoretical simulations. Consequently, the Li–S cells utilizing the EPDB-CgCP booster offer high-rate performance (775 mAh g^{-1} at 3 C) and long cycling life (800 cycles at 2 C). Increasing the sulfur mass loading to 5.7 mg cm^{-2}, the cell with EPDB-CgCP still exhibits a promising areal capacity of 3.2 mAh cm^{-2}. An appealing capacity of 647 mAh g^{-1} is also achieved after 80 cycles under the ambient temperature to 0 °C, suggesting the fast desolvation ability propelled by EPDB-CgCP diffusion booster. This work points out a feasible strategy for improving the conversion kinetics of LiPSs by simultaneously catalyzing and sieving the solvation structure of Li^+, raising a bright way to realize high-performance Li–S batteries.

Supporting Information

Supporting Information is available from the Wiley Online Library or from the author.

Acknowledgements

X.Z. and X.L. contributed equally to this work. This work was financially supported by the National Key R&D Program (2021YFA1201503), National Natural Science Foundation of China (nos. 22075081, 21972164, 22279161, 11874089, 11904187, and 12264038), the Fundamental Research Funds for the Central Universities (JKD01231701), Shanghai Sailing Program of China (23YF1408900), the Natural Science Foundation of Jiangsu Province (BK 20210130), and Natural Science Foundation of Inner Mongolia (no. 2022MS01013). J.W. thanks to the fellowship awarded by the Alexander von Humboldt Foundation. Y.Z. thanks to the Shanghai Super Postdoctoral Incentive Program. The authors also thank to the technical support from Nano-X, Suzhou Institute of Nano-Tech and Nano-Bionics, Chinese Academy of Sciences.

Conflict of Interest

The authors declare no conflict of interest.

Data Availability Statement

The data that support the findings of this study are available from the corresponding author upon reasonable request.

Keywords

electrocatalysis modulation, Li^+ diffusion booster, lithium–sulfur batteries, solvation structures, sulfur conversion kinetics

Received: March 7, 2023
Revised: April 15, 2023
Published online: May 19, 2023

[1] a) Q. Kang, Z. Zhuang, Y. Li, Y. Zuo, J. Wang, Y. Liu, C. Shi, J. Chen, H. Li, P. Jiang, X. Huang, *Nano Res.* **2023**, 10.1007/s12274-023-5478-4 b) W. Yang, J. Xiao, Y. Ma, S. Cui, P. Zhang, P. Zhai, L. Meng, X. Wang, Y. Wei, Z. Du, B. Li, Z. Sun, S. Yang, Q. Zhang, Y. Gong, *Adv. Energy Mater.* **2019**, *9*, 1803137; c) Z. Cao, Y. Zhang, Y. Cui, J. Gu, Z. Du, Y. Shi, K. Shen, H. Chen, B. Li, S. Yang, *Energy Environ. Mater.* **2021**, *5*, 45.

[2] a) W. Wang, K. Xi, B. Li, H. Li, S. Liu, J. Wang, H. Zhao, H. Li, A. Abdelkader, X. Gao, G. Li, *Adv. Energy Mater.* **2022**, *12*, 2200160; b) Y. Lin, W. Tang, S. Wu, Y. Zhang, Z. Kong, C. Shen, Y. Wang, L. Zhan, L. Ling, *Chem. Eng. J.* **2023**, *452*, 139091.

[3] a) J. Zhang, L. Zhou, H. Ming, Y. Wu, W. Wahyudi, Z. Cao, L. Cavallo, L. Wang, J. Ming, *Chem. Commun.* **2019**, *55*, 5713; b) J. Wang, L. Li, H. Hu, H. Hu, Q. Guan, M. Huang, L. Jia, H. Adenusi, K. Tian, J. Zhang, S. Passerini, H. Lin, *ACS Nano* **2022**, *16*, 17729.

[4] a) B. Li, S. Li, J. Liu, B. Wang, S. Yang, *Nano Lett.* **2015**, *15*, 3073;. b) T. Yang, J. Xia, Z. Piao, L. Yang, S. Zhang, Y. Xing, G. Zhou, *ACS Nano* **2021**, *15*, 13901; c) Y. Zhang, G. Xu, Q. Kang, L. Zhan, W. Tang, Y. Yu, K. Shen, H. Wang, X. Chu, J. Wang, S. Zhao, Y. Wang, L. Ling, S. Yang, *J. Mater. Chem. A* **2019**, *7*, 16812; d) B. Li, S. Li, J. Xu, S. Yang, *Energy Environ. Sci.* **2016**, *9*, 2025.

[5] S. Wu, X. Li, Y. Zhang, Q. Guan, J. Wang, C. Shen, H. Lin, J. Wang, Y. Wang, L. Zhan, L. Ling, *Nano Res.* **2023**, 10.1007/s12274-023-5532-2

[6] a) W. Yao, W. Zheng, J. Xu, C. Tian, K. Han, W. Sun, S. Xiao, *ACS Nano* **2021**, *15*, 7114; b) X. Li, Q. Guan, Z. Zhuang, Y. Zhang, Y. Lin, J. Wang, C. Shen, H. Lin, Y. Wang, L. Zhan, L. Ling, *ACS Nano* **2023**, *17*,1653.

[7] a) J. Zhang, C. You, H. Lin, J. Wang, *Energy Environ. Mater.* **2022**, *5*, 731; b) J. Wang, L. Jia, J. Zhong, Q. Xiao, C. Wang, K. Zang, H. Liu,

H. Zheng, J. Luo, J. Yang, H. Fan, W. Duan, Y. Wu, H. Lin, Y. Zhang, *Energy Storage Mater.* **2019**, *18*, 246.
[8] T. Li, D. Cai, S. Yang, Y. Dong, S. Yu, C. Liang, X. Zhou, Y. Ge, K. Xiao, H. Nie, Z. Yang, *Adv. Mater.* **2022**, *34*, 2207074.
[9] K. Ding, C. Xu, Z. Peng, X. Long, J. Shi, Z. Li, Y. Zhang, J. Lai, L. Chen, Y. P. Cai, Q. Zheng, *ACS Appl. Mater. Interfaces* **2022**, *14*, 44470.
[10] H. Yang, Y. Qiao, Z. Chang, P. He, H. Zhou, *Angew. Chem., Int. Ed.* **2021**, *60*, 17726.
[11] a) X. Fan, L. Chen, X. Ji, T. Deng, S. Hou, J. Chen, J. Zheng, F. Wang, J. Jiang, K. Xu, C. Wang, *Chem* **2018**, *4*, 174; b) Y. Yamada, J. Wang, S. Ko, E. Watanabe, A. Yamada, *Nat. Energy* **2019**, *4*, 269; c) Z. Zeng, V. Murugesan, K. Han, X. Jiang, Y. Cao, L. Xiao, X. Ai, H. Yang, J. Zhang, M. Sushko, J. Liu, *Nat. Energy* **2018**, *3*, 674.
[12] Z. Chang, H. Yang, Y. Qiao, X. Zhu, P. He, H. Zhou, *Adv. Mater.* **2022**, *34*, 2201339.
[13] L. Li, H. Tu, J. Wang, M. Wang, W. Li, X. Li, F. Ye, Q. Guan, F. Zhu, Y. Zhang, Y. Hu, C. Yan, H. Lin, M. Liu, *Adv. Funct. Mater.* **2023**, *33*, 2212499.
[14] a) Y. Jiang, J. Liang, L. Yue, Y. Luo, Q. Liu, Q. Kong, X. Kong, A. Asiri, K. Zhou, X. Sun, *J. Colloid Interface Sci.* **2021**, *604*, 319; b) F. Zhou, R. Wang, S. He, X. Liu, S. Liu, H. Shao, X. Liu, Z. Xiao, J. Liu, *Adv. Funct. Mater.* **2023**, *33*, 2211124.
[15] a) K. Xu, *Chem. Rev.* **2004**, *104*, 4303; b) K. Xu, *Chem. Rev.* **2014**, *114*, 11503.
[16] J. Wang, J. Zhang, S. Cheng, J. Yang, Y. Xi, X. Hou, Q. Xiao, H. Lin, *Nano Lett.* **2021**, *21*, 3245.
[17] Y. Wang, P. Liang, H. Yang, W. Li, Z. Wang, Z. Liu, J. Wang, X. Shen, *Mater. Today Energy* **2020**, *17*, 100423.
[18] Z. Kong, Q. Liu, X. Liu, Y. Wang, C. Shen, L. Zhan, *Appl. Surf. Sci.* **2021**, *546*, 148914.
[19] S. Ahn, M. J. Klein, A. Manthiram, *Adv. Energy Mater.* **2017**, *7*, 1601979.
[20] H. Xia, L. Zan, G. Qu, Y. Tu, H. Dong, Y. Wei, K. Zhu, Y. Yu, Y. Hu, D. Deng, J. Zhang, *Energy Environ. Sci.* **2022**, *15*, 771.
[21] W. Henderson, D. Seo, S. Han, O. Borodin, *J. Electrochem. Soc.* **2020**, *167*, 110551.
[22] a) J. Wu, T. Zhou, B. Zhong, Q. Wang, W. Liu, H. Zhou, *ACS Appl. Mater. Interfaces* **2022**, *14*, 27873; b) S. Chen, J. Zheng, D. Mei, K. Han, M. Engelhard, W. Zhao, W. Xu, J. Liu, J. Zhang, *Adv. Mater.* **2018**, *30*, 1706102.
[23] J. Xu, F. Yu, J. Hua, W. Tang, C. Yang, S. Hu, S. Zhao, X. Zhang, Z. Xin, D. Niu, *Chem. Eng. J.* **2020**, *392*, 123694.
[24] B. Hu, J. Xu, Z. Fan, C. Xu, S. Han, J. Zhang, L. Ma, B. Ding, Z. Zhuang, Q. Kang, X. Zhang, *Adv. Energy Mater.* **2023**, *13*, 2203540.
[25] a) J. Xu, S. An, X. Song, Y. Cao, N. Wang, X. Qiu, Y. Zhang, J. Chen, X. Duan, J. Huang, W. Li, Y. Wang, *Adv. Mater.* **2021**, *33*, 2105178; b) Q. Kang, Y. Li, Z. Zhuang, D. Wang, C. Zhi, P. Jiang, X. Huang, *J. Energy Chem.* **2022**, *69*, 194.
[26] a) Z. Piao, P. Xiao, R. Luo, J. Ma, R. Gao, C. Li, J. Tan, K. Yu, G. Zhou, H. Cheng, *Adv. Mater.* **2022**, *34*, 2108400; b) L. Yang, X. Li, K. Pei, W. You, X. Liu, H. Xia, Y. Wang, R. Che, *Adv. Funct. Mater.* **2021**, *31*, 2103971.
[27] a) Z. Du, Y. Guo, H. Wang, J. Gu, Y. Zhang, Z. Cheng, B. Li, S. Li, S. Yang, *ACS Nano* **2021**, *15*, 19275; b) J. Wang, L. Jia, S. Duan, H. Liu, Q. Xiao, T. Li, H. Fan, K. Feng, J. Yang, Q. Wang, M. Liu, J. Zhong, W. Duan, H. Lin, Y. Zhang, *Energy Storage Mater.* **2020**, *28*, 375.
[28] Z. Du, C. Wu, Y. Chen, Q. Zhu, Y. Cui, H. Wang, Y. Zhang, X. Chen, J. Shang, B. Li, W. Chen, C. Liu, S. Yang, *Adv. Energy Mater.* **2021**, *12*, 2103228.
[29] D. Zhang, S. Wang, R. Hu, J. Gu, Y. Cui, B. Li, W. Chen, C. Liu, J. Shang, S. Yang, *Adv. Funct. Mater.* **2020**, *30*, 2002471.
[30] R. Li, J. He, M. Lei, M. Yang, C. Li, *Chem. Eng. J.* **2022**, *446*, 137294.
[31] W. Yao, C. Tian, C. Yang, J. Xu, Y. Meng, I. Manke, N. Chen, Z. Wu, L. Zhan, Y. Wang, R. J. Chen, *Adv. Mater.* **2022**, *34*, 2106370.
[32] W. Zhou, D. Zhao, Q. Wu, B. Fan, J. Dan, A. Han, L. Ma, X. Zhang, L. Li, *J. Colloid Interface Sci.* **2021**, *603*, 1.
[33] a) G. Liang, L. Yang, X. Xiong, K. Pei, X. Zhao, C. Wang, W. You, X. Liu, X. Zhang, R. Che, *Adv. Funct. Mater.* **2022**, *32*, 2206129; b) X. Xiong, L. Yang, G. Liang, Z. Liu, Z. Yang, R. Zhang, C. Wang, R. Che, *Adv. Energy Mater.* **2022**, *12*, 2201967.
[34] a) D. Lu, X. Wang, Y. Hu, L. Yue, Z. Shao, W. Zhou, L. Chen, W. Wang, Y. Li, *Adv. Funct. Mater.* **2023**, *33*, 2212689; b) C. Zhou, M. Hong, N. Hu, J. Yang, W. Zhu, L. Kong, M. Li, *Adv. Funct. Mater.* **2023**, *33*, 2213310; c) Z. Zhuang, Q. Kang, D. Wang, Y. Li, *Nano Res.* **2020**, *13*, 1856; d) L. Yang, G. Liang, H. Cao, S. Ma, X. Liu, X. Li, G. Chen, W. You, C. Lin, R. Che, *Adv. Funct. Mater.* **2022**, *32*, 2105026; e) L. Yang, X. Xiong, G. Liang, X. Li, C. Wang, W. You, X. Zhao, X. Liu, R. Che, *Adv. Mater.* **2022**, *34*, 2200914.
[35] J. Xu, H. Zhang, F. Yu, Y. Cao, M. Liao, X. Dong, Y. Wang, *Angew. Chem., Int. Ed.* **2022**, *61*, e202211933.
[36] Z. Wang, B. Zhang, S. Liu, G. Li, T. Yan, X. Gao, *Adv. Funct. Mater.* **2022**, *32*, 2200893.
[37] Y. Zhang, Z. Cao, S. Liu, Z. Du, Y. Cui, J. Gu, Y. Shi, B. Li, S. Yang, *Adv. Energy Mater.* **2022**, *12*, 2103979.
[38] a) C. Li, Q. Zhang, J. Sheng, B. Chen, R. Gao, Z. Piao, X. Zhong, Z. Han, Y. Zhu, J. Wang, G. Zhou, H. Cheng, *Energy Environ. Sci.* **2022**, *15*, 4289; b) G. Liang, L. Yang, Q. Han, G. Chen, C. Lin, Y. Chen, L. Luo, X. Liu, Y. Li, R. Che, *Adv. Energy Mater.* **2020**, *10*, 1904267; c) L. Yang, X. Zhu, X. Li, X. Zhao, K. Pei, W. You, X. Li, Y. Chen, C. Lin, R. Che, *Adv. Energy Mater.* **2019**, *9*, 1902174; d) X. Xiong, L. Yang, G. Liang, C. Wang, G. Chen, Z. Yang, R. Che, *Adv. Funct. Mater.* **2022**, *32*, 2106911.
[39] W. Hua, H. Li, C. Pei, J. Xia, Y. Sun, C. Zhang, W. Lv, Y. Tao, Y. Jiao, B. Zhang, S. Qiao, Y. Wan, Q. Yang, *Adv. Mater.* **2021**, *33*, 2101006.
[40] H. Xia, L. Zan, P. Yuan, G. Qu, H. Dong, Y. Wei, Y. Yu, Z. Wei, W. Yan, J. Hu, D. Deng, J. Zhang, *Angew. Chem., Int. Ed.* **2023**, *62*, e202218282.
[41] L. Zhang, T. Qian, X. Zhu, Z. Hu, M. Wang, L. Zhang, T. Jiang, J. Tian, C. Yan, *Chem. Soc. Rev.* **2019**, *48*, 5432.
[42] C. Zhao, G. Xu, Z. Yu, L. Zhang, I. Hwang, Y. Mo, Y. Ren, L. Cheng, C. Sun, Y. Ren, X. Zuo, J. Li, S. Sun, K. Amine, T. Zhao, *Nat. Nanotechnol.* **2021**, *16*, 166.
[43] D. Luo, C. Li, Y. Zhang, Q. Ma, C. Ma, Y. Nie, M. Li, X. Weng, R. Huang, Y. Zhao, L. Shui, X. Wang, Z. Chen, *Adv. Mater.* **2022**, *34*, 2105541.